JOURNAL OF GEOPHYSICAL RESEARCH, VOL. 100, NO. E5, PAGES 9389–9400, MAY 25, 1995

Backscatter model for the unusual radar properties of the Greenland Ice Sheet

Eric Rignot

Jet Propulsion Laboratory, California Institute of Technology, Pasadena

Abstract. A number of planetary objects exhibit large radar reflectivity and polarization ratios, and more recently, a similar behavior has been observed over a vast portion of the Earth's surface: the percolation facies of the Greenland Ice Sheet. Surface-based ranging radar data and snow stratigraphy studies demonstrated that the radar properties of that portion of Greenland are caused by enhanced scattering from massive, large, solid-ice bodies buried in the top few meters of the dry, cold, clean snowy surface of the ice sheet and created by seasonal melting and refreezing events. Here, we model the icy inclusions as randomly oriented, discrete, noninteracting, dielectric cylinders embedded in a transparent snow medium. An exact analytical solution is used to compute the scattered field from the cylinders. Using this model, we correctly predict the polarimetric radar observations gathered by an airborne imaging system at three wavelengths (5.6, 24, and 68 cm), between 19° and 65° incidence angle. The diameter and number density of the cylinders that are inferred from the radar data using the model are consistent with in situ observations of the icy inclusions. The large radar reflectivity and polarization ratios are interpreted as arising from internal reflections of the radar signals in the icy inclusions that first-order external reflection models fail to predict. The results compare favorably with predictions from the coherent backscatter or weak localization theory and may provide a complementary framework for interpreting exotic radar echoes from other planetary objects.

1. Introduction

Since the early 1970s, unusual radar properties have been detected from the icy Galilean satellites, Europa, Ganymede, and Callisto (EGC) by Earth-based radar telescopes [*Ostro*, 1993; *Ostro et al.*, 1992]. Their radar reflectivity is several orders of magnitude larger than that recorded for comets, the Moon, the inner planets, and nonmetallic asteroids. Their circular polarization ratio, μ_C (i.e. RR/RL or LL/LR, where LR is the echo power measured receiving left-circular (L) polarization while transmitting right-circular (R) polarization) is greater than unity. Hence, in contrast to most other natural targets, the scattering largely preserves the helicity of the transmitted signal. The linear polarization ratio, μ_L (i.e. HV/HH or VH/VV, where H means horizontal and V means vertical), is also much larger than that recorded for other planetary objects. Similar unusual radar characteristics have been recorded from the Mars residual south polar cap [*Muhleman et al.*, 1991; *Harmon et al.*, 1992], portions of Titan [*Muhleman et al.*, 1990], polar caps on Mercury [*Slade et al.*, 1992; *Harmon and Slade*, 1992], and portions of Venus [*Tryka and Muhleman*, 1992]. First-order scattering models fail to explain the scattering behavior of these objects or are inconsistent with their formation history and geology [*Ostro and Shoemaker*, 1990]. Only recently, the coherent backscatter effect [e.g., *van Albada et al.*, 1990; *MacKintosh and John*, 1988], also known as weak localization theory, was suggested as a likely explanation for these radar echoes which was both consistent with their geology and capable of explaining their large radar reflectivity and polarization ratios [*Hapke*, 1990]. Coherent backscatter arises from constructive interferences in the radar backscattering direction between electromagnetic signals traveling along identical but time-reversed paths. In the presence of wavelength-sized objects, closely spaced ($\sim \lambda$) scattering heterogeneities of low refractive index embedded in a nearly transparent medium (e.g., water-ice) are required for the coherent backscatter effect to dominate. When the scattering objects are much larger than the observing wavelength, coherent backscatter is noticeable only if the particle concentration is low [*Kuga and Ishimaru*, 1989; *Mishchenko*, 1992a]. Validation of the coherent backscatter theory is however limited to laboratory-controlled experiments [*O'Donnell and Mendez*, 1987; *MacKintosh et al.*, 1989; *Hapke and Blewett*, 1991] due to the absence of detailed, in situ observations of

Paper number 95JE00485.
0148-0227/95/95JE-00485$05.00

the subsurface configurations responsible for the radar echoes from these planetary objects.

More recently, a similar behavior has been observed over a vast portion of the Earth's surface: the percolation facies of the Greenland Ice Sheet [*Rignot et al.*, 1993]. The percolation facies represent a major fraction of the Greenland Ice Sheet which itself covers a 1,726,400 km^2 area [*Benson*, 1962]. It had been known for several years that the percolation facies exhibited an unusual strong type of radar backscattering [*Swift et al.*, 1985], but it was not until 1991 that calibrated radar data could be gathered in that region, at three different wavelengths, multiple incidence angles, and most important, with the full polarimetry, using the NASA/Jet Propulsion Laboratory AIRSAR airborne synthetic-aperture radar imaging system [*van Zyl et al.*, 1992]. The AIRSAR results showed that the circular and linear polarization ratios of the Greenland percolation facies are extremely large and comparable in magnitude to the largest ratios recorded for EGC. The radar reflectivity of the Greenland percolation facies is also one of the largest values recorded at the surface of the Earth at centimetric wavelengths. Analysis of signals recorded at 5.7- and 2.2-cm wavelength by a surface-based ranging radar deployed on the ice sheet at the time of the AIRSAR over flight demonstrated that the unusual radar echoes are caused by strong scattering from the first annual layer of ice bodies buried at depth (0.4 to 2.0 m, depending on the time of the year) in the cold, dry, porous, snowy upper surface of the ice sheet [*Jezek and Gogineni*, 1992; *Jezek et al.*, 1994]. Off nadir, radar returns from the surface of the ice sheet, as well as from deeper layers of ice bodies, are as much as 10 dB weaker than that from the first layer of ice bodies.

These icy formations are well known to glaciologists [*Benson*, 1962; *Pfeffer et al.*, 1991; *Jezek and Gogineni*, 1992; *Echelmeyer et al.*, 1992]. They form in the top few meters of the snowy surface of the ice sheet as a result of seasonal melting and refreezing events. They differ from the glacial ice, 50 to 100 m underneath the surface, that results from diagenetic processes transforming snow into solid ice. The physical processes leading to the formation of the icy inclusions have been studied in great detail [*Benson*, 1962; *Pfeffer et al.*, 1990]. At these high elevations ($\geq$2000 m above mean sea level) and high northern latitudes ($\geq$63°N) snow remains at temperatures <0°C throughout the summer, except at point locations where meltwater can percolate downwards, along active channels, through much of the previous winter's accumulated snow. Meltwater refreezes at depth ($\leq$1 m) when it encounters a discontinuity in hydraulic conductivity associated with a fine-to-coarse grain size transition [*Pfeffer and Humphrey*, 1992]. When active, the percolation channels appear slushy. When refreezing, they form a network of ice pipes, lenses and layers that distribute laterally, sometimes over great distances. Ice lenses are lens-shaped layers which pinch out laterally, parallel to the firn (old snow) strata; while ice pipes are pipelike, vertically extending masses reminiscent of the percolation channels which feed ice lenses and layers. Ice layers are typically several millimeters to a few centimeters thick and extend over several tens of meters. Ice pipes (Figure 1) and ice lenses are 2-20 cm wide and 10-100 cm long [*Jezek et al.*, 1994].

Ice layers also form at lower elevations, in the so-called soaked-snow facies [*Benson*, 1962], but the snow there reaches 0°C in the summer and is therefore moist and not transparent to the radar signals. Hence, the radar signals cannot interact with the buried ice bodies. In winter, the melted snow refreezes to form a superimposed ice zone which acts as a continuous, thick, impermeable horizon of low radar reflectivity and polarization ratios. Conversely, summer melting rarely occurs at higher elevations, in the dry-snow facies [*Benson*, 1962]. No icy formations are found in the top meters of the snowy surface and the radar reflectivity and polarization ratios are as low as in the soaked-snow facies.

Using the icy Galilean satellites as an analogy, the coherent backscatter effect was suggested as a possible

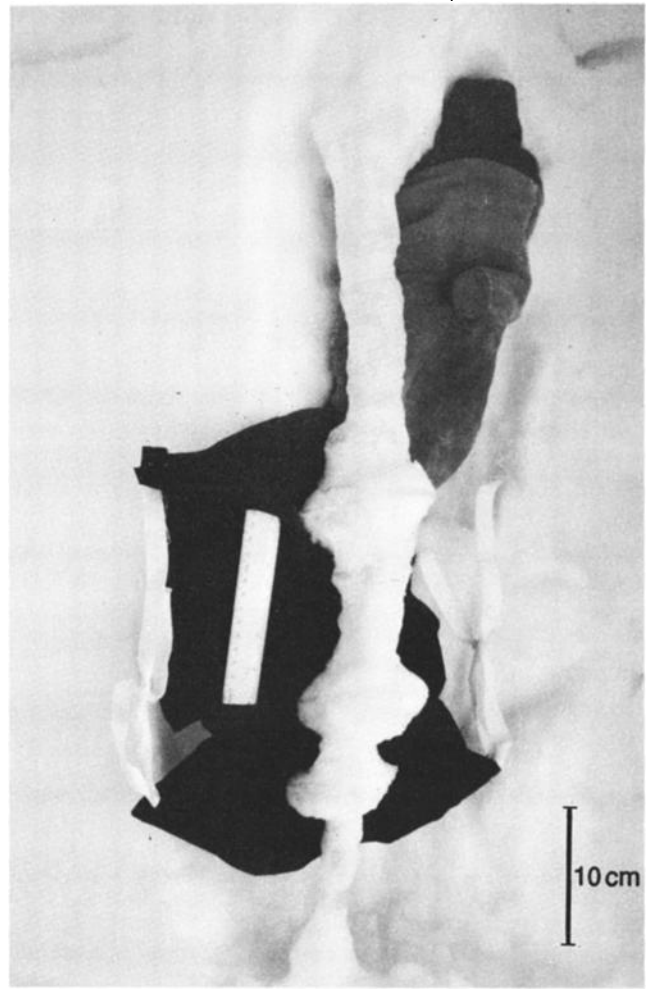

Figure 1. Photograph of an ice pipe found at 1.80 m depth in the firn at Crawford Point on June 11, 1991. The ice pipe is 70 cm long, with a diameter varying between 3 and 10 cm (courtesy of K. Jezek, OSU).

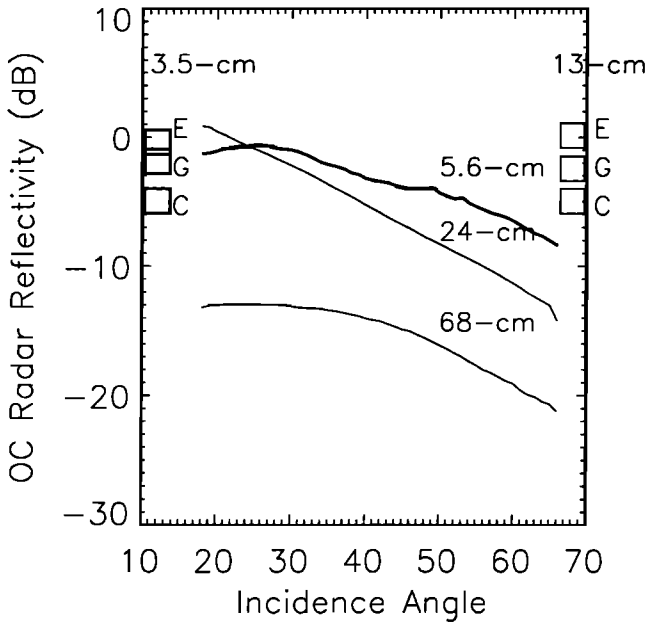

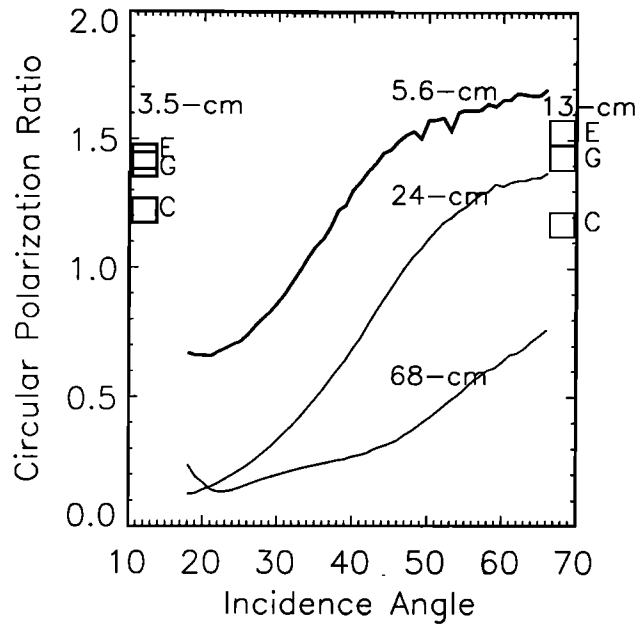

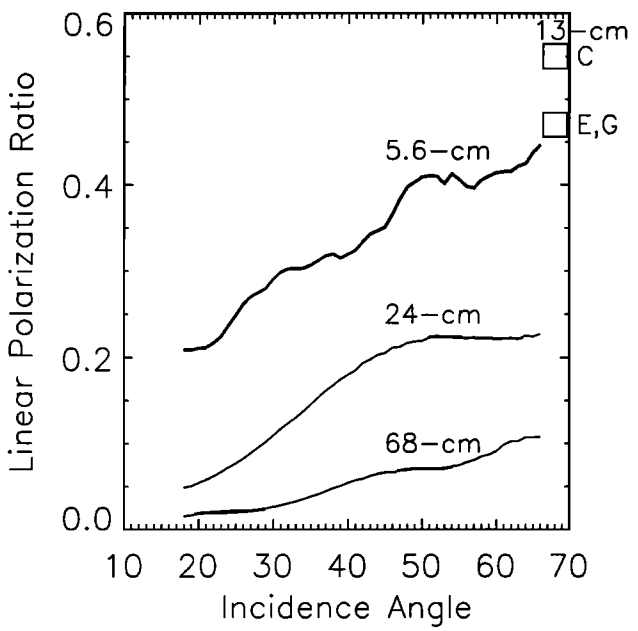

Figure 2. OC radar reflectivity σ^0_{RL}, circular polarization ratio μ_C, and linear polarization ratio μ_L recorded at Crawford Point at 5.6, 24 and 68 cm as a function of the incidence angle θ. The plot also includes disk-integrated values of σ^0_{OC} and μ_C recorded at 3.5 and 13 cm for EGC [*Ostro et al.*, 1992]; and μ_L for EGC at 13 cm only [*Ostro et al.*, 1980]. The data points for EGC, arbitrarily placed at 11° incidence (3.5 cm) and 69° incidence (13 cm), are disk-integrated values.

explanation for the radar properties of the Greenland percolation facies [*Rignot et al.*, 1993]. The upper few meters of the ice sheet are sufficiently transparent to allow long photon path length and higher order scattering, and contain an abundance of solid-ice scatterers comparable in size to the radar wavelength. These properties suggest that coherent backscatter could dominate the radar echoes. Here, we present a revision of our earlier hypothesis that the Greenland radar echoes are explained by the coherent backscatter effect. Our approach is based on the modeling of the subsurface configuration responsible for the Greenland radar echoes and on an examination of the radar properties of the icy scatterers. The results are used to address the following three issues: Is there a backscatter model that can quantitatively mimic the radar properties of Greenland at several radar frequencies, all polarizations, and various incidence angles? What kind of geophysical information can we extract from the radar data using this model? What can we learn from this study in terms of interpreting unusual radar echoes from other planetary surfaces?

2. Radar Observations

The NASA/Jet Propulsion Laboratory airborne SAR (AIRSAR) operates a synthetic-aperture imaging radar simultaneously at three wavelengths (λ = 5.6 cm (C band); 24 cm (L band); and 68 cm (P band)), recording the complete scattering matrix at each wavelength by alternatively transmitting and receiving vertical and horizontal-polarized radar signals. With an operating altitude of about 9000 m above ground and a 10-km swath, the radar system collects images where the incidence angle of the illumination varies typically between 19° in near range (closest point to the radar) to 65° in far range (furthest point from the radar). The data are processed into a 10 km x 10 km quadrant, with a pixel spacing of about 12 m on the ground in both azimuth (along-track) and range (across-track) directions.

The radar data gathered at Crawford Point (69.87°N, 47.11°W) (see Figure 1 of *Rignot et al.*, [1993]) were averaged along-track and plotted as a function of polarization, frequency, and incidence angle in Figure 2. The OC (opposite sense circular) radar reflectivity and the polarization ratios are computed, respectively, as

$$\sigma^o_{OC} = RL \; ; \quad \mu_C = RR/RL \; ; \quad \mu_L = HV/HH. \quad (1)$$

The polarization ratios are defined such that for pure reflection off a perfectly smooth dielectric surface $\mu_C = 0$ and $\mu_L = 0$ because a pure reflection reverses the handedness of the helicity of the incident circular polarization (hence RR or LL = 0), but preserves the orientation of the incident linear polarization (hence HV or VH = 0). In the case of volume scattering from randomly distributed dipoles, we have $\mu_C = 1$ and $\mu_L = 1/3$ [*Long*, 1965]. For pure double reflections off a perfectly smooth dielectric dihedral whose lower face is horizontal, $\mu_C = \infty$ (because RL = 0) and $\mu_L = 0$ (because HV = 0).

Also shown in Figure 2 are the disk-integrated measures of the radar reflectivity and polarization ratios of EGC at 3.5- and 13-cm from *Ostro et al.* [1980, 1992]. Both EGC and the Greenland percolation facies exhibit strong radar reflectivity, $\mu_C > 1$ and $\mu_L > 1/3$. Most natural terrestrial surfaces and Inner Solar System planetary bodies exhibit lower radar reflectivities, $\mu_C << 1$ and $\mu_L << 1/3$.

To illustrate the discussion with real examples, we listed several AIRSAR measurements of heavily vegetated areas (forests) and very rough surfaces (lava flows) in Table 1. Both situations are expected to yield large radar reflectivity and polarization ratios via multiple scattering interactions. In broadleaf-upland tropical rain forest in Belize (-17.58°N, 89.0°W) [*Freeman et al.*, 1992], σ^o_{OC} is lower than that recorded for Greenland at the same incidence (Figure 2), and $\mu_C \approx 1$ and $\mu_L \approx 1/3$ at 24 and 68 cm. These values of μ_C and μ_L are consistent with scattering dominance by the volume of tree branches and foliage of the forest canopy which act as randomly distributed thin cylinders or dipoles. At 5.6 cm, $\mu_C < 1$ and $\mu_L < 1/3$ because the branches are no longer thin compared with the observing wavelength. There are, however, numerous cases of forested areas where $\mu_C > 1$ at the longer wavelengths. For instance, in palm-tree communities of the Manu National Park tropical rain forest, in Peru (-11.98°N, 70.8°W) AIRSAR measured $\mu_C > 1.5$ and $\mu_L < 0.1$ at 68 cm (Table 1), with σ^o_{OC} much lower than that for Greenland. Similarly, in the flooded floodplain forests of the Bonanza Creek Experimental Forest (64.75°N, -148°W), near Fairbanks, Alaska, $\mu_C > 1$ at 24- and 68-cm, σ^o_{OC} is large, and $\mu_L < 1/3$. We interpret this behavior as being due to double-bounce reflections of the radar signals from the tree trunks to the wet ground back to the radar direction. Double-bounce scattering increases with increasing tree height [*van Zyl*, 1993] (hence is largest for tall forests), increasing wetness of the ground layers and/or of the tree trunks (hence largest for flooded forests), and increasing radar penetration (hence largest at the longer wavelengths and/or for sparse forests). Double-bounce reflections yield $\mu_C >> 1$ and $\mu_L = 0$ unless the tree trunks are slanted or damaged [*van Zyl*, 1993]. These examples illustrate that situations where $\mu_C > 1$ are not uncommon in forested areas and are explainable in terms of trunk-ground scattering interactions. The observed radar reflectivity remains, however, much lower than that recorded in Greenland.

Table 1. OC Radar Reflectivity σ^o_{OC}, Circular Polarization Ratio μ_C, Linear Polarization Ratio μ_L, HH/VV Ratio, and HH-VV Phase Difference $\phi_{HH-VV} \pm$ Standard Deviation, of Seven Sites Imaged by the NASA/JPL AIRSAR Instrument.

Site and CM Number	λ, cm	θ, deg	σ^o_{OC}	μ_C	μ_L	HH/VV	ϕ_{HH-VV}, deg
Belize CM1213	5.6	45	0.22	0.73	0.26	1.07	-5 ± 36
(94:140,374:402)	24	45	0.11	1.04	0.31	0.92	-2 ± 65
	68	45	0.05	1.16	0.28	1.01	15 ± 77
Manu CM3700	5.6	40	0.16	0.57	0.22	0.93	0 ± 16
(110:154,656:670)	24	40	0.11	1.17	0.24	1.18	8 ± 59
	68	40	0.08	1.57	0.12	2.67	71 ±100
Bonanza Creek CM3136	5.6	34	0.16	0.85	0.18	1.38	13 ± 35
(68:114,258:286)	24	34	0.17	1.71	0.14	1.72	84 ± 77
	68	34	0.21	1.72	0.08	1.39	114 ± 28
Lunar Crater CM2061b	5.6	21	0.22	0.29	0.13	0.86	2 ± 15
(606:642,202:224)	24	21	0.14	0.35	0.16	0.87	3 ± 18
	68	21	0.07	0.36	0.13	1.28	9 ± 15
SP Flow CM0189	5.6	37	NA	1.36	0.30	1.38	14 ± 21
(770:820,408:448)	24	37	NA	1.03	0.33	1.03	9 ± 51
	68	37	NA	0.43	0.16	0.88	13 ± 21
Inyo Domes CM3793	5.6	41	0.23	0.32	0.15	0.89	5 ± 10
(606:684,390:432)	24	41	0.16	0.60	0.23	1.01	-1 ± 13
	68	41	0.17	0.87	0.33	0.77	4 ± 22
Greenland CM3206	5.6	42	0.35	1.61	0.41	0.87	-25 ± 80
(230:346,506:562)	24	42	0.12	1.22	0.24	1.19	-29 ± 56
	68	42	0.02	0.48	0.08	2.29	-1 ± 10

The CM number refers to the nomenclature used to archive the AIRSAR images, λ (cm) is the observing wavelength, and θ is the incidence angle. The box of image pixels used to extract the average radar characteristics in each AIRSAR image is indicated in the first colum in (row:column) format. For SP flow, σ^o_{OC} is omitted (NA, not applicable) because it could not be calibrated with confidence, but the polarization ratios are correct. The 5.6-cm SP flow data were corrected for an erroneous antenna pattern correction introduced during the original processing of the SAR data.

Enhanced radar backscatter and strong depolarization of the radar signals may also occur on surfaces that are very rough at the scale of the radar wavelength, for instance through multiple reflections of the radar signals on the large facets of blocky structure of the surface. Several authors [*Fahnenstock et al.*, 1993; *Jezek et al.*, 1994] argued that the unusual radar properties of the Greenland percolation facies are caused by surface scattering from the rough ice layers. To determine whether this is a valid explanation, we examined the radar response of several types of very rough surfaces and experimented with theoretical backscatter models.

Lava flows are good examples of rough terrestrial terrain. Table 1 shows the radar characteristics of Qb3 lava flow (quaternary volcanic basalt flow, younger type) of the Lunar Crater Volcanic Field (38.47°N, 116.07°W), in the Mojave Desert, Nevada [*Evans et al.*, 1992; *Scott and Trask*, 1971]. The surface rms height was estimated from stereo imagery to be about 24 cm, the largest value recorded in the area. At 30° incidence, σ^o_{OC} is much lower than that recorded in Greenland (Figure 2), $\mu_C < 1$ and $\mu_L < 1/3$. This example suggests that rough surfaces are unlikely to exhibit exotic radar characteristics. Radar observations of the basaltic lava flows of the Kilauea Volcano, Hawaii, confirm this presumption [*Campbell et al.*, 1993]. Recent AIRSAR observations of the silicic lava flows and domes in the Inyo volcanic chain in the Eastern Sierra of California (37.7°N, 119.1°W) [*Plaut et al.*, 1993, 1995] also show that even when the surface rms height exceeds 80 cm, the corresponding radar signatures are not exotic (Table 1). Circular polarization ratios greater than unity have however been reported for SP flow of northern Arizona (35.8°N, 117.42°W) [*Campbell et al.*, 1993] (Table 1). SP flow is a blocky basaltic andesite lava deposit whose surface is characterized by roughly cubical blocks 10-100 cm in size and whose sides are smooth on the scale of a few centimeters. Interestingly, $\mu_L \approx 1/3$ in SP flow (Table 1). These large polarization ratios cannot be caused by the coherent backscatter effect because the refractive index of rock in air is too large to yield coherent backscattering [*Peters*, 1992; *Mishchenko*, 1992b, 1992c]. A more likely explanation is that scattering is dominated by multiple double-bounce reflections on the dihedrals formed by the large facets of the blocky structure of the surface. As $\mu_L > 1/3$ at 5.6 and 24 cm, the dihedrals must be systematically randomly oriented, otherwise $\mu_L = 0$ (see (5)). The lower values of μ_C and μ_L at 68 cm are consistent with block sizes of less than 1 m. Similarly, the HH/VV ratios are close to 1 (Table 1), as predicted from double-bounce scattering from randomly oriented dihedrals (see (7)).

Radar scattering models for randomly rough dielectric surfaces are usually not valid over the complete range of surface roughness values encountered in natural terrain settings. One of the most comprehensive models to date is the integral equation method (IEM) [*Fung et al.*, 1992]. The IEM model unites the small perturbation model [*Rice*, 1951] for slightly rough surfaces and the Kirchhoff theory for very rough surfaces. We tested the IEM model using the roughness values measured with a mechanical comb gauge at the surface of an ice layer (3-cm rms height and 3-cm correlation length [*Jezek et al.*, 1994]). The results, shown in Figure 3, illustrate the incompatibility of the model predictions with the AIRSAR observations. The contrast between 5.6- and 24-cm echoes is overpredicted and the modeled radar reflectivity at small incidence is several decibels below that recorded for Greenland. Hence, the IEM model predictions, together with numerous radar observations of rough terrestrial surfaces (Table 1), strongly suggest that surface scattering from the ice layers cannot explain the radar characteristics of Greenland.

3. A Backscatter Model for the Percolation Facies

One common deficiency of many backscatter models is that they are only approximations to the exact solution of the scattered field from the scattering objects. Higher-order modes of interactions of the radar signals with the objects are simply ignored. Although this simplification is justified for most natural targets, it is not the case for Greenland, where higher-order internal reflection terms are predominant.

The exact solution of the scattered field from dielectric objects exists for a few simple objects including spheres, cylinders, and spheroids [*Bohren and Huffman*, 1983; *Asano and Sato*, 1980]. Here, we use discrete, dielectric cylinders to model the icy inclusions of the percolation facies. The ice layers are not represented, as they probably are too thin compared with the observing wavelength to scatter the incoming radar sig-

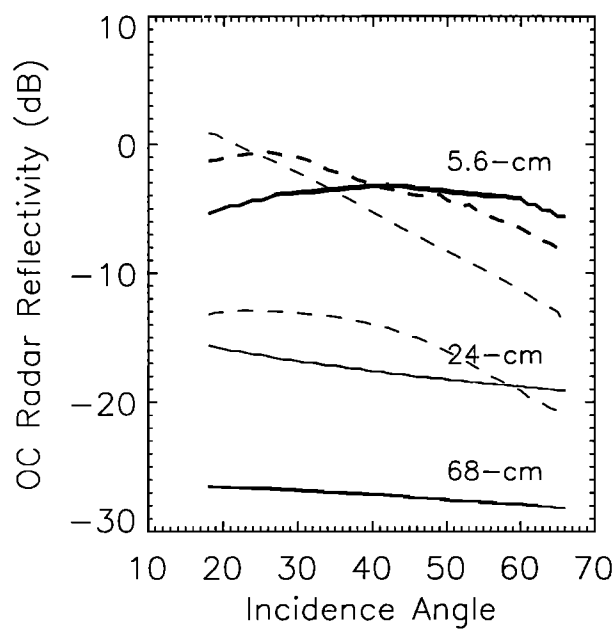

Figure 3. Backscatter model predictions of the radar reflectivity at HH-polarization from the IEM theory (continuous thick lines) compared with the AIRSAR measurements (dashed lines) at 5.6, 24, and 68 cm versus the incidence angle θ. The surface rms height is 3 cm with a 3-cm correlation length.

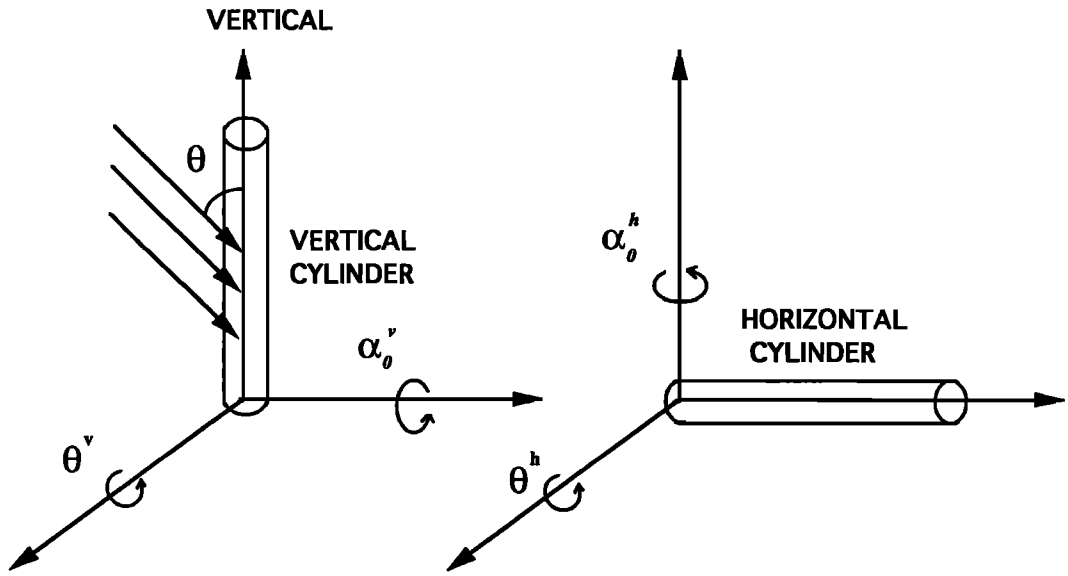

Figure 4. Configuration of the vertical and horizontal cylinders used in the backscatter model, with the definition of the incidence angle, θ, the orientation angles of the vertical cylinders, θ^v and α_o^v, and the orientation angles of the horizontal cylinders, θ^h and α_o^h.

nals efficiently. The ice pipes are modeled as vertically oriented cylinders. Each cylinder has a radius r_v, and N_v is the number of vertical cylinders per meter square. Because the ice pipes are not strictly vertical in reality, the vertical cylinders are randomly oriented within $\pm\theta^v$ in the plane of incidence and $\pm\alpha_o^v$ in the vertical plane (Figure 4). As the role of θ^v is merely to smooth out the trend in radar backscatter of the cylinders versus the incidence angle, its value is noncritical. We chose $\theta^v = 5^o$ because it provided a reasonable amount of smoothing of the backscatter curves, while remaining compatible with the field observations. The angle α_o^v is not known a priori and is used as a free model parameter. Similarly, the ice lenses are modeled as N_h horizontal cylinders of radius r_h, randomly oriented within $\pm\theta^h$ in the plane of incidence and $\pm\alpha_o^h$ in the horizontal plane (Figure 4). We fixed $\theta^h = 5^o$. Since the cylinders are randomly oriented in the horizontal plane, we have $\alpha_o^h = 90^o$.

Because the ice pipes and lenses are typically separated by much more than one wavelength, the scattered field from these objects is uncorrelated. As a result, total radar backscatter from a distribution of discrete, dielectric cylinders is computed as the incoherent sum of the scattered field from the noninteracting, discrete cylinders.

The absorption properties of dry, cold snow are assumed to be negligible. Snow is nearly transparent to radar signals at those wavelengths. Snow, however, steepens the incidence angle of the radar illumination through refraction of the radar signals at the air-snow interface, reduces the dielectric constant of water-ice in dry air ($\epsilon = 3.2$) to a lower value corresponding to water-ice in dry snow ($\epsilon = 1.78$ for a snow density of 0.4 kg/m^3 [*Tiuri et al.*, 1984]), and reduces the effective wavelength of the radar signals by $\sqrt{\epsilon}$, here 25%.

The exact scattering matrix for a dielectric cylinder of infinite length is given by *Bohren and Huffman*, [1983]. The analytical solution for a finite cylinder is computed by scaling the solution for the infinite cylinder by a shape factor, f,

$$f = \frac{kh}{\pi} \sin_c(k\ h\ \cos\ \theta) \tag{2}$$

where k is the wavenumber in the propagation medium, h is the cylinder length, θ is the incidence angle, and $\sin_c(x) = \sin(x)/x$. If the cylinder length varies randomly by a quantity $\pm\epsilon_h$, the average solution for the scattered field intensity is obtained by averaging f^2 between $h - \epsilon_h$ and $h + \epsilon_h$. When $\epsilon_h >> \lambda$, the effective value of f^2 is

$$< f^2 >= \frac{1}{2\pi^2 \cos^2\theta}, \tag{3}$$

which is independent of both h and ϵ_h. This result means that when the cylinder length fluctuates by $\sim \lambda$ or more, the mean cylinder length has no influence on the radar properties of the cylinder. Given the typical sizes of ice pipes and lenses, this condition is easily satisfied at 5.6 and 24 cm. We assume it also applies at 68 cm. Hence, the shape factor f^2 is only a function of the incidence angle.

We now examine how to compute the scattered field from randomly distributed discrete, dielectric cylinders, given the solution for one cylinder. The scattering matrix $[S] = [S_{HH}, S_{HV}, S_{VH}, S_{VV}]$ of a single, dielectric, vertical cylinder is

$$[S] = [a, 0, 0, b] \tag{4}$$

where a and b are complex numbers whose magnitude and phases are functions of the cylinder dielec-

tric constant and diameter [*Bohren and Huffman*, 1983]. To calculate the average covariance matrix for vertical cylinders randomly oriented in the vertical plane between $-\alpha_o^v$ and $+\alpha_o^v$, we apply a rotation operator to $[S]$, compute the cross-products of the rotated scattering matrix $[S][S^*]^t$ (where the asterisk means complex conjugate and superscript t means transpose), and average the results between $-\alpha_o^v$ and $+\alpha_o^v$. The results are

$$< S_{HV} S_{HV}* > = | a - b |^2 I_{22} \quad (5)$$

$$< S_{HH} S_{HH}* > = (| a |^2 + | b |^2) I_4 + 2Re(a^* b) I_{22} \quad (6)$$

$$< S_{VV} S_{VV}* > = < S_{HH} S_{HH}* > \quad (7)$$

$$< S_{HH} S_{VV}* > = (| a |^2 + | b |^2) I_{22} + 2Re(a^* b) I_4 \quad (8)$$

$$I_4 = \int_{-\alpha_o^v}^{\alpha_o^v} \cos^4(\alpha) d\alpha$$

$$I_{22} = \int_{-\alpha_o^v}^{\alpha_o^v} \cos^2(\alpha) \sin^2(\alpha) d\alpha \quad (9)$$

At circular polarization, the cross products are

$$< S_{RR} S_{RR}* >= \frac{1}{2}(I_4 + I_{22}) \mid a - b \mid^2 \quad (10)$$

$$< S_{LL} S_{LL}* >=< S_{RR} S_{RR}* > \quad (11)$$

$$< S_{RL} S_{RL}* >= \frac{1}{2}(I_4 - I_{22}) \mid a + b \mid^2 + I_{22} \mid a - b \mid^2 \quad (12)$$

The polarization ratios are simply deduced from (5)-(7) and (10)-(12). Equations (5)-(12) also apply to horizontal cylinders randomly oriented in the horizontal plane, provided that α_0^v is replaced by $\alpha_o^h = 90^o$, and θ is replaced by 90^o - θ (Figure 4).

When $\alpha_o^v = 90^o$ and b approaches zero (thin cylinder limit), we find $\mu_C = 1$ and $\mu_L = 1/3$, as for the case of scattering from a forest canopy where branches are thin compared to the wavelength. When $| b |$ approaches $| a |$ (thick cylinder limit), we find $\mu_C = 0$ and $\mu_L = 0$, as expected since $[S]$ becomes the identify matrix. When $a = -1$ and $b = 1$ (case of a dihedral reflector), we find $\mu_C = (I_4 + I_{22})/(2\ I_{22})$ and $\mu_L = I_{22}/(I_4 - I_{22})$. Hence, large polarization ratios may be obtained from a distribution of randomly oriented dihedrals. For instance, $\mu_C = 2$ and $\mu_L = 0.5$ when $\alpha_0^v = 90^o$, perhaps explaining the radar echoes of SP flow.

When $\alpha_o^v = 0$ (purely vertical cylinders), we find $\mu_L = 0$ and $\mu_C =| (a - b)/(a + b) |^2$. Hence, vertical cylinders do not generate any cross-polarized intensity unless they are systematically randomly oriented in the vertical plane. We assume that the randomness in orientation of the ice pipes reflects spatial irregularities in shape and orientation of the ice pipes along their longest dimension at a scale comparable to or larger than the wavelength (Figure 1).

Using this backscatter model, we predict large polarization ratios for the icy inclusions. To illustrate this result, Figures 5a-5c show the radar reflectivity and polarization ratios of various sized cylinders as a function of the size parameter $(k\ .\ r)$, where k is the wavenumber and r is the cylinder radius. Narrow peaks in μ_C and μ_L observed for particular values of $(k\ .\ r)$ coincide with a $\pm 180^o$ phase difference between HH- and VV-polarization. These peaks are caused by internal reflections of the radar signals in the cylinders, which include the glory ray effect [*Bohren and Huffman*, 1983] as well as other types of internal reflections included in the exact analytical solution to the scattered field. Internal reflections are the only type of returns that would cause a large phase difference between H-polarized and V-polarized radar signals. As the refractive index of the cylinder increases, the magnitude of these internal reflections is expected to decrease, as shown in Figures 5d-5f for water-ice cylinders in vacuum (refractive index ~1.8). Hence, the refractive index of the cylinders needs to be small enough (typically <1.6) to yield strong internal reflections and $\mu_C > 1$, and the cylinders need to be randomly oriented to yield large values of μ_L.

Model predictions for an ensemble of horizontal and vertical cylinders are shown in Figure 6 along with the AIRSAR data. Several model parameters were tuned to best fit the model predictions with the AIRSAR data. These parameters are r_h, r_v, N_h, N_v and α_o^v. The parameter tuning was done as follows. Test values for r_v were selected among those producing a peak in polarization ratios (Figure 5) because the model showed that the value of r_v controls the polarization ratios of the ensemble of horizontal and vertical cylinders at high incidence. Since μ_C and μ_L are low at low incidence, the value of r_h is less critical. We chose $r_h = r_v = r$ to simplify the procedure. The selected average cylinder radius was then used to generate a normal distribution of cylinder radius, with a relatively small standard deviation (see caption to Figure 6). The best results were usually obtained with $r \sim \lambda/2$, which is not surprising, since it corresponds to wavelength-sized objects. Given r, the number densities were selected to best fit σ_{OC}^o because the model showed that σ_{OC}^o is proportional to N_h at small incidence and to N_v at high incidence. Note here that with vertical or horizontal cylinders only ($N_v = 0$ or $N_h = 0$), the model could not predict the correct trends in μ_C and μ_L versus the incidence angle. Both horizontal and vertical cylinders are needed to match the AIRSAR observations. The angle α_o^v was finally selected to properly balance μ_L and μ_C, as the model showed that these ratios vary in opposite directions when α_o^v changes. Because of the large number of constraints provided by the multiparameter radar data, only one set of r, N_v, N_h and α_o^v values was found to yield a good agreement with the AIRSAR data, at each radar wavelength. The HH/VV ratio of the ensemble of cylinders is predicted to be 1 (see (7)), in agreement with the 5.6- and 24-cm data (Table 1), and is therefore not discussed. Finally, the HH-VV phase difference (fifth independent parameter of the covariance matrix) is predicted to be close to zero by the model, but with a large standard deviation caused by internal reflections (Figure 5), which is consistent with the AIRSAR observations of large standard deviations of the HH-VV phase difference (Table 1).

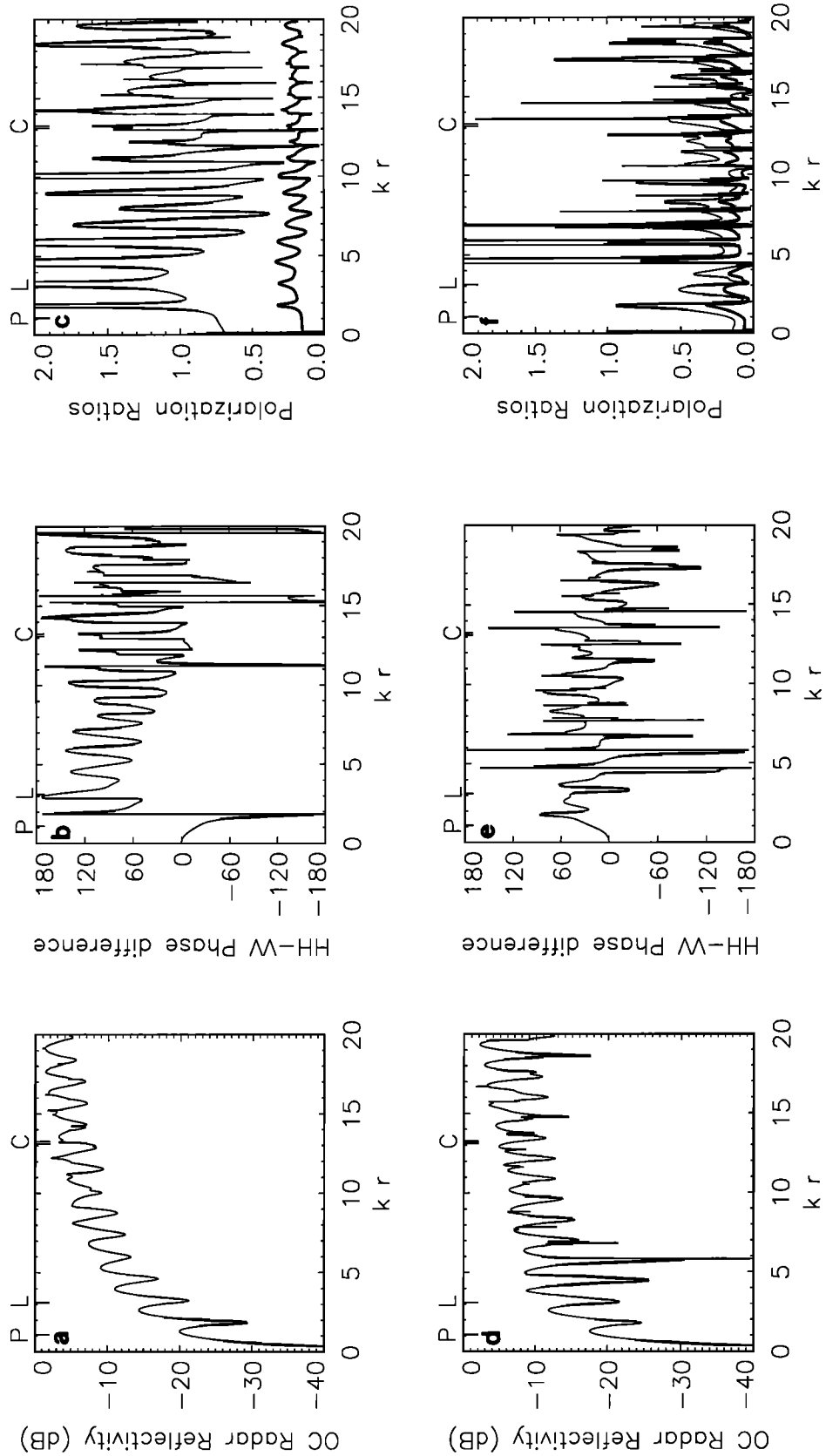

Figure 5. (a) Polarization ratios (μ_L in continuous thick lines), (b) OC radar reflectivity and (c) HH-VV phase difference for a single, dielectric, finite cylinder with $\epsilon_r = 1.78$ (water-ice in dry snow) as a function of the size parameter (kr), where k is the wavenumber and r is the cylinder radius. (d)-(f) Same quantities plotted for $\epsilon_r = 3.2$ (water-ice in vacuum). The values of the size parameter (kr) for $r = 3.1$ cm are indicated in (a) through (f) at 5.6- (letter C), 24- (letter L), and 68-cm (letter P) wavelengths.

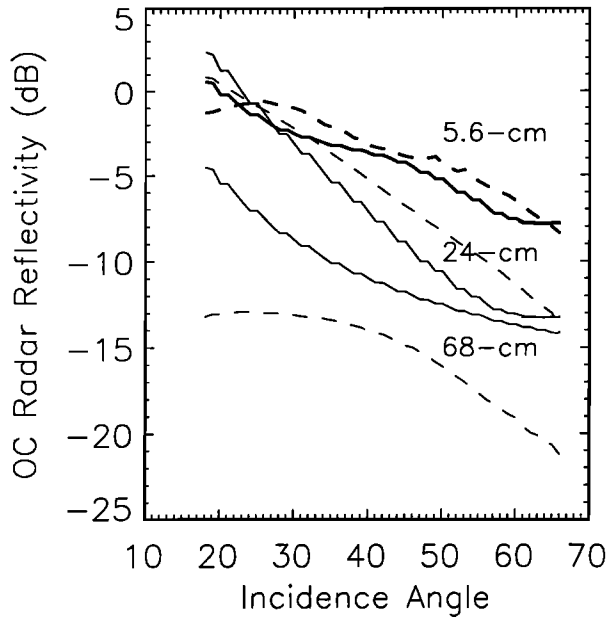

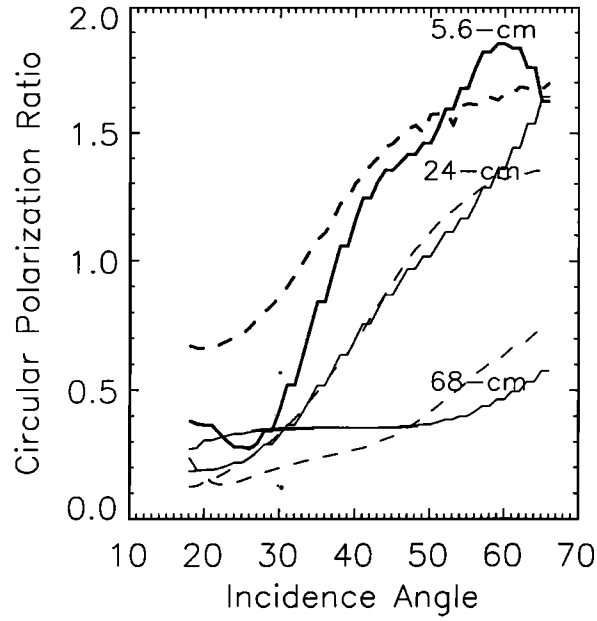

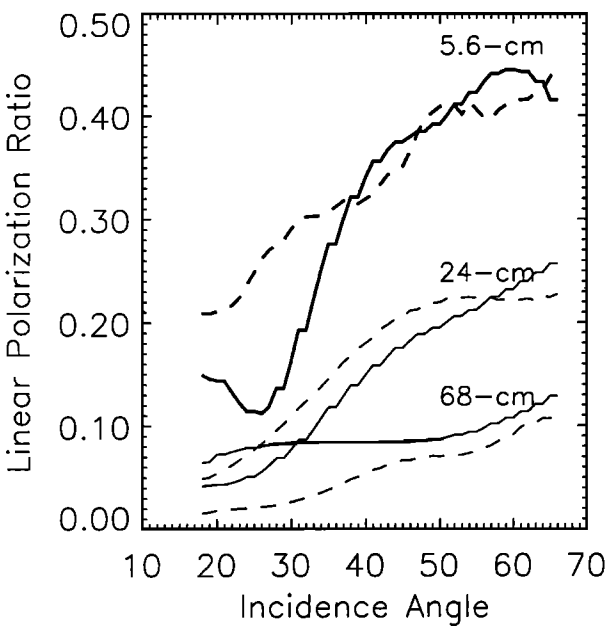

Figure 6. Model predictions for discrete, nearly vertical and horizontal, dielectric cylinders (continuous lines) compared with the AIRSAR measurements (dashed lines) at 5.6-, 24-, and 68-cm wavelengths. At 5.6 cm (thick lines), we used $r = 3.1 \pm 0.05$ cm; $\alpha_o^v = 70°$; $N_v = 5$ cyl/m^2; $N_h = 1.5$ cyl/m^2. At 24- and 68-cm, we used $r = 8.9 \pm 0.05$ cm; $\alpha_o^v = 50°$; $N_v = 1$ cyl/m^2; $N_h = 3$ cyl/m^2.

At 5.6-cm wavelength, the model predictions are most accurate with $r = 3.1$ cm, $N_v = 5$ cyl/m^2 (cylinder per square meter), $\alpha_o^v = 70°$, and $N_h = 1.5$ cyl/m^2. The value $r = 2.2$ cm produces low estimates of σ_{OC}^o when μ_C and μ_L are correct, whereas the larger value, $r = 4.0$ cm, produces correct estimates of σ_{OC}^o but low polarization ratios. Snow stratigraphy studies reveal that ice pipes are several tens of centimeters long and of diameter varying anywhere between 2-4 cm and 10-20 cm. The number density of icy inclusions was not measured per se (such measurement would require the digging of a large number of snow pits), but snow stratigraphy studies and *Benson*'s [1962] earlier results suggest that a few pipes and lenses per square meter is a reasonable number. Hence, the model results are qualitatively consistent with in situ observations.

At 24 cm, we found $r = 8.9$ cm, $N_v = 1$ cyl/m^2, $\alpha_o^v = 50°$, and $N_h = 3$ cyl/m^2. Field observations suggest this value may be at the limit of being too large to represent an ice pipe. We could not match the AIRSAR data at both 5.6 and 24 cm using a single normal distribution of the cylinder radius with a large standard deviation. The model requires a bimodal distribution of r to yield a good agreement with both wavelengths. We do not know whether a bimodal distribution of the cylinder radius is realistic. The 24-cm radar signals probably interact with more than one layer of ice bodies, yielding more complex interactions than those accounted for in our model. Unfortunately, no surface-based radar ranging data were gathered at that wavelength to determine whether the dominant scatterers are still localized in the first annual layer of ice bodies.

At 68 cm, the polarization ratios and radar reflectivity are always low for r between 3.1 and 8.9 cm and would only be large for $r \sim 15$-20 cm. Icy inclusions are never this large. Both the model and the 68-cm radar observations are therefore consistent with the typical size of the inclusions. An example of model prediction at 68 cm is shown in Figure 6 using the model parameters optimized at 24 cm. The agreement with the AIRSAR data is reasonable, except for the radar reflectivity. One possibility is that (3) does not apply at 68 cm (~68-cm fluctuations in length of the ice pipes is excessive). The polarization ratios are unaffected, but the radar

reflectivity could be overestimated. Another possibility is that scattering is of a different nature at 68 cm. This result is suggested by HH/VV >> 1 and the low value of the standard deviation of the HH-VV phase difference at 68 cm (Table 1). As ice becomes nearly transparent at that wavelength, radar signals probably interact with much deeper layers of solid ice.

4. Discussion

The modeling results demonstrate that internal reflection of radar signals in horizontal and vertical, discrete, solid-ice inclusions buried in the snowy, radar-transparent, surface of the ice sheet can explain the extraordinary radar properties of the Greenland percolation facies. The agreement with the AIRSAR data is excellent at 5.6 cm. At the longer wavelengths, the source of scattering is less certain in the absence of surface-based radar ranging measurements. Nevertheless, the backscatter model provides reasonable estimates of the size and number density of icy inclusions. More detailed and extensive in-situ observations of icy inclusions are required to establish on a firmer basis the development of a quantitative inversion model for icy surfaces. The length of the cylinders cannot be estimated from the model. Additional constraints on the aspect ratio of the ice bodies are necessary to estimate the volume of ice bodies from the radar data. Measuring the volume of water-ice retained in the ice sheet after summer melt in the percolation facies would be of considerable interest to estimating the mass balance of the Greenland Ice Sheet [*Pfeffer et al.*, 1990].

Several backscatter models have been proposed in the past to explain unusual radar echoes from planetary surfaces. The mode-decoupled refraction scattering [*Hagfors et al., 1985; Eshelman, 1986*] would not apply for Greenland because it requires exotic subsurface structures that do not exist. The total-internal reflection model [*Goldstein and Green,* 1980] is similar to the present model. Here, we use a complete analytical solution of the scattered field, and henceforth can predict under which circumstances internal reflections may dominate other forms of scattering and by what amount. For example, we predict that internal reflections in pure water-ice cylinders in vacuum would not likely yield $\mu_C > 1$ (Figure 5). As a result, the radar echoes of Ganymede may not be solely caused by internal reflections in a crazed and fissued water-ice regolith with a large number of ice-vacuum interfaces.

The coherent backscatter effect is most effective with wavelength-sized scatterers, in which case it requires closely spaced, forward scatterers of low refractive index in a weakly absorbing medium [e.g., *van Albada et al.*, 1990; *Peters,* 1992; *Mishchenko,* 1992b, 1992c]. There is no requirement on the geometrical shape of the scatterers. The present model also requires scatterers of low refractive index embedded in a weakly absorbing medium, but not necessarily closely spaced. In situ observations of the subsurface configuration of the ice sheet show that icy inclusions are often separated by many wavelengths, in which case the coherent backscatter effect should not take place. In addition, model predictions from the coherent backscatter theory using spherical scatterers suggest that μ_C and μ_L should decrease with an increasing incidence angle (Figures 6,9,15,18 of *Mishchenko,* [1992c]), whereas the AIRSAR measurements show an opposite trend. Hence, we conclude that internal reflections from a monolayer of discrete icy inclusions is a better explanation for the unusual radar echoes recorded in Greenland than coherent backscattering from a random distribution of icy inclusions.

For other planets, the conclusions may be different. On the surface of Venus, internal reflections or coherent backscattering may dominate external reflections in places where the propagation medium is nearly transparent. If the medium is not transparent, as in the case of lava flows, double-bounce scattering over randomly distributed dihedrals formed by the large facets of blocky structure of lava flows is a more likely scattering mechanism for explaining the exotic radar signatures recorded by the Magellan spacecraft at 12 cm. This form of scattering is our favored explanation for the radar echoes recorded in SP flow and in the lava flows and domes of the Inyo volcanic chain.

On water-ice terrain, multiple external reflections will not dominate because of the low Fresnel reflection coefficient of water-ice. Exotic echoes are therefore more likely caused by internal reflections or coherent backscattering from within the icy regolith volume than by external reflections at the surface of the regolith. In the case of EGC, partial melting and percolation facies will not occur because of the low temperatures, and the subsurface configurations responsible for the EGC echoes are probably quite different from those in Greenland. Instead of monolayers of cylinder-shaped icy inclusions, scatterers on EGC could be discrete pieces of cratering ejecta, randomly distributed in the icy regolith, with no preferred orientation (because μ_C shows hardly any variations across the planetary disk), a wider distribution in size than in Greenland (because μ_C does not vary significantly and remains greater than unity between 3.5 cm and 70 cm on EGC; while μ_C decreases significantly from 5.6 to 24 cm in Greenland and $\mu_C < 1$ at 68 cm), and a low refractive index comparable to that of water-ice in dry, cold snow (1.33). Internal reflections occur in dielectric cylinders of low refractive index, in randomly oriented spheroids [*Asano and Sato,* 1980; *Mishchenko and Travis,* 1994], and could probably occur in random modulations in dielectric constant in a smoothly heterogeneous icy regolith [*Ostro and Shoemaker,* 1990]. To resolve the issue of whether coherent backscattering or internal reflections dominate scattering, bi-static radar observations of the planets would be of considerable interest. With regards to the extraction of geophysical information from the radar data, the Greenland results suggest that observations of planetary surfaces should be actively pursued and include an even larger variety of observing wavelengths to characterize more completely

the responsible scattering processes and their electrical and structural attributes.

Acknowledgments. This work was carried out at the Jet Propulsion Laboratory, California Institute of Technology, under contract with the Polar Research Branch of the National Aeronautics and Space Administration. I thank Jakob van Zyl for stimulating discussions during the course of this study and for providing his computer code calculating the scattering matrix of a finite, dielectric cylinder. I also thank Bruce Hapke, Bruce Campbell, Mike Mishchenko, and Steven Ostro for providing extremely useful reviews of the manuscript; Kenneth Jezek and Carl Benson for valuable discussions on snow stratigraphy studies in Greenland; Jian Cheng Shi for providing his implementation of the IEM model; and Jeffrey Plaut for sharing his AIRSAR observations of the Inyo-Mono domes in advance of publication.

References

Asano, S., and M. Sato, Light scattering by randomly oriented spheroidal particles, *Appl. Opt., 19*, 962-974, 1980.

Benson, C., Stratigraphic studies of the snow and firn of the Greenland ice sheet, Res. Rep. *70*, U.S. Army Snow Ice and Permafrost Res. Estab., 1962.

Bohren, C. F., and D. R. Huffman, *Absorption and Scattering of Light by Small Particles*, John Wiley, New York, 1983.

Campbell, B.A., R.E. Arvidson, and M.K. Shepard, Radar polarization properties of volcanic and playa surfaces: Applications to terrestrial remote sensing and Venus data interpretation, *J. Geophys. Res., 98*, 17,099-17,113, 1993.

Echelmeyer, K., W.D. Harrison, T.S. Clarke, and C. Benson, Surficial glaciology of Jakobshavns Isbrae, West Greenland, Part II, Ablation, accumulation and temperature, *J. Glaciol., 38*, 169, 1992.

Eshelman, V.R., Mode decoupling during retrorefraction as an explanation for bizarre radar echoes from icy moons, *Nature, 319*, 755-757, 1986.

Evans, D.L., T.G. Farr, and J.J. van Zyl, Estimates of surface roughness derived from synthetic-aperture radar (SAR) data, *IEEE Trans. Geosci. Remote Sens., 30*, 382-389, 1992.

Fahnenstock, M., R. Bindschadler, R. Kwok, and K. Jezek, Greenland Ice Sheet surface properties and ice dynamics from ERS-1 SAR imagery, *Science, 262*, 1530-1534, 1993.

Freeman, A., S. Durden, and R. Zimmermann, Mapping of sub-tropical vegetation using multi-frequency, multipolarization SAR data, in *Proceedings of the International Geoscience and Remote Sensing Symposium, Houston, Texas, May 26-29*, p. 1686, IEEE, New York, 1992.

Fung, A.K., L. Zongqian, and K.S. Chen, Backscattering from a randomly rough dielectric surface, *IEEE Trans. Geosci. Remote Sens., 30*, 356-369, 1992.

Goldstein, R.M., and R.R. Green, Ganymede: Radar surface characteristics, *Science, 207*, 179, 1980.

Hagfors, T., T. Gold, and M. Ierkic, Refraction scattering as origin of the anomalous radar returns of Jupiter's satellites, *Nature, 315*, 637-640, 1985.

Hapke, B., Coherent backscatter and the radar characteristics of outer planet satellites, *Icarus, 88*, 407-417, 1990.

Hapke, B., and D. Blewett, Coherent backscattering model for the unusual radar reflectivity of icy satellites, *Nature, 352*, 46, 1991.

Harmon, J.K., M.A. Slade, and R.S. Hudson, Mars radar scattering: Arecibo/Goldstone results at 12.6-cm and 3.5-cm wavelengths, *Icarus, 98*, 240, 1992.

Harmon, J.K. and M.A. Slade, Radar mapping of Mercury: Full-disk images and polar anomalies, *Science, 258*, 640, 1992.

Jezek, K.C., and S.P. Gogineni, Microwave remote sensing of the Greenland Ice Sheet, *IEEE Geosci. Remote Sens. Soc. Newslett., 9*, 6-10, 1992.

Jezek, K.C., S.P. Gogineni, and M. Shanbleh, Radar measurements of melt zones on the Greenland Ice Sheet, *Geophys. Res. Lett., 21*, 33-36, 1994.

Kuga, Y., and A. Ishimaru, Backscattering enhancement by randomly distributed very large particles, *Appl. Opt., 28*, 2165-2169, 1989.

Long, M.W., On the polarization and the wavelength dependence of sea echo, *IEEE Antennas Propag., 14*, 749, 1965.

MacKintosh, F.C., and S. John, Coherent backscattering of light in the presence of time-reversal-noninvariant and parity-nonconserving media, *Phys. Rev. B, 37*, 1884, 1988.

MacKintosh, F.C., J.X. Zhu, D.J. Pine, and D.A. Weitz, Polarization memory of multiply scattered light, *Phys. Rev. B, 40*, 2383, 1989.

Mishchenko, M.I., The angular width of the coherent backscatter opposition effect: An application to icy outer planet satellites, *Astrophys. Space Sci., 194*, 327-333, 1992a.

Mishchenko, M.I., Enhanced backscattering of polarized light from discrete random media: Calculations in exactly the backscattering direction, *J. Opt. Soc. Am., 9*, 978, 1992b.

Mishchenko, M.I., Polarization characteristics of the coherent backscatter opposition effect, *Earth Moon Planets, 58*, 127-144, 1992c.

Mishchenko, M.I., and L.D. Travis, Light scattering by polydispersions of randomly oriented spheroids with sizes comparable to wavelengths of observation, *Appl. Opt., 33*, 7206-7225, 1994.

Muhleman, D.O., B.J. Butler, A.W. Grossman, and M.A. Slade, Radar images of Mars, *Science, 253*, 1508, 1991.

Muhleman, D.O., A.W. Grossman, B.J. Butler, and M.A. Slade, Radar reflectivity of Titan, *Science, 248*, 975, 1990.

O'Donnell, K., and E. Mendez, Experimental study of scattering from characterized random surfaces, *J. Opt. Soc. Am. A, 4*, 1194-1205, 1987.

Ostro, S.J., Planetary radar astronomy, *Rev. Mod. Phys.*, 65, 1235-1279, 1993.

Ostro, S.J., and E.M. Shoemaker, The extraordinary radar echoes from Europa, Ganymede, and Callisto: A geological perspective, *Icarus, 85*, 335, 1990.

Ostro, S.J., D.B. Campbell, G.H. Pettengill, and I.I. Shapiro, Radar observations of the icy Galilean satellites, *Icarus, 44*, 431-440, 1980.

Ostro, S.J. et al., Europa, Ganymede, and Callisto: New radar results from Arecibo and Goldstone, *J. Geophys. Res., 97*, 18,227-18,244, 1992.

Peters, K.J., The coherent backscatter effect: a vector formulation accounting for polarization and absorption effects of small and large scatterers, *Phys. Rev. B, 46*, 801, 1992.

Pfeffer, W.T. and N.F. Humphrey, Initiation of ice piping and ice layering in subfreezing snow, (abstract) *Eos Trans. AGU, 73*(43), Fall Meeting suppl., 194, 1992.

Pfeffer, W.T., T.H. Illangasekare and M.F. Meier, Analysis and modeling of melt-water refreezing in dry snow, *J. Glaciol., 36*, 238-246, 1990.

Pfeffer, W.T., M.F. Meier, and T.H. Illangasekare, Retention of Greenland runoff by refreezing: Implications for projected future sea level change, *J. Geophys. Res., 96*, 22,117-22,124, 1991.

Plaut, J.J., E. R. Stofan, D.A. Crown, and S.W. Anderson, Steep-sided volcanic domes on Venus and Earth: Macroscale geometry from remote sensing and field measurements, (abstract) *Eos Trans. AGU, 74* (43), Fall Meeting suppl., 378, 1993.

Plaut, J.J., E.R. Stofan, S.W. Anderson and D.A. Crown, The unique radar properties of silicic lava flows and domes, in Summaries of the Fifth Annual JPL Airborne Earth Science Workshop, Jet Propulsion Laboratory, Pasadena, CA, Jan. 23-26, 1995, vol. 3, Edited by J. van Zyl, *JPL Publ., 95-1*, 35-38, 1995.

Rice, S. O., Reflection of electromagnetic waves from slightly rough surfaces, *Commun. Pure Appl. Math., 4*, 351-378, 1951.

Rignot, E., S.J. Ostro, J.J. van Zyl and K.C. Jezek, Unusual radar echoes from the Greenland Ice Sheet, *Science, 261*, 1710-1713, 1993.

Scott, D.H., and N.J. Trask, Geology of the Lunar Crater volcanic field, Nye County, NV, *U.S. Geol. Surv. Prof. Pap., 599-I*, 1971.

Slade, M.A., B.J. Butler, and D.O. Muhleman, Mercury radar imaging: evidence for polar ice, *Science, 252*, 252, 1992.

Swift, C.T., P.S. Hayes, and J.S. Herd, Airborne microwave measurements of the southern Greenland ice sheet, *J. Geophys. Res., 90*, 1983-1994, 1985.

Tiuri, M., A.H. Sihvola, E.G. Nyfors, and M.T. Hallikainen, The complex dielectric constant of snow at microwave frequencies, *IEEE J. Oceanic Eng., 9*, 377-382, 1984.

Tryka, K.A., and D.O. Muhleman, Reflection and emission properties on Venus: Alpha Regio, *J. Geophys. Res., 97*, 13,379, 1992.

van Albada, M.P., M.B. van der Mark and A. Lagendijk, Experiments on weak localization of light and their interpretation, in *Scattering and Localization of Classical Waves in Random Media*, edited by P. Sheng, p. 97, World Scientific, Singapore, 1990.

van Zyl, J. J., The effect of topography on radar scattering from vegetated areas, *IEEE Trans. Geosci. Remote Sens., 31*, 153-160, 1993.

van Zyl, J. J., R. Carande, Y. Lou, T. Miller, and K. Wheeler, The NASA/JPL three-frequency polarimetric AIRSAR system, in *Proceedings International Geoscience and Remote Sensing Symposium, Houston, Texas, May 26-29*, pp. 649-651, IEEE, New York, 1992.

Eric Rignot, Jet Propulsion Laboratory, Mail Stop 300-243, 4800 Oak Grove Drive, Pasadena, CA 91109-8099. (e-mail: eric@adelie.jpl.nasa.gov)

(Received September 28, 1994; revised February 3, 1995; accepted February 7, 1995.)